

## Nonperturbing electron beam probe to diagnose charged particle beams

John A. Pasour and Mai T. Ngo

Citation: *Rev. Sci. Instrum.* **63**, 3027 (1992); doi: 10.1063/1.1142603

View online: <http://dx.doi.org/10.1063/1.1142603>

View Table of Contents: <http://rsi.aip.org/resource/1/RSINAK/v63/i5>

Published by the [American Institute of Physics](#).

---

### Related Articles

A short pulse (7 $\mu$ s FWHM) and high repetition rate (dc-5kHz) cantilever piezovalve for pulsed atomic and molecular beams

*Rev. Sci. Instrum.* **80**, 113303 (2009)

Absolute metastable atom-atom collision cross section measurements using a magneto-optical trap

*Rev. Sci. Instrum.* **78**, 073102 (2007)

A new ultrafast technique for measuring the terahertz dynamics of chiral molecules: The theory of optical heterodyne-detected Raman-induced Kerr optical activity

*J. Chem. Phys.* **122**, 244503 (2005)

Improved method for measuring absolute O<sub>2</sub>(a<sup>1</sup> $\Delta$ <sub>g</sub>) concentration by O<sub>2</sub>(a<sup>1</sup> $\Delta$ <sub>g</sub>→X<sup>3</sup> $\Sigma$ <sub>g</sub><sup>-</sup>) IR radiation

*Rev. Sci. Instrum.* **75**, 4455 (2004)

Chaotic particle motion and beam halo formation induced by image-charge effects in a small-aperture alternating-gradient focusing system

*Phys. Plasmas* **10**, 4203 (2003)

---

### Additional information on *Rev. Sci. Instrum.*


Journal Homepage: <http://rsi.aip.org>

Journal Information: [http://rsi.aip.org/about/about\\_the\\_journal](http://rsi.aip.org/about/about_the_journal)


Top downloads: [http://rsi.aip.org/features/most\\_downloaded](http://rsi.aip.org/features/most_downloaded)

Information for Authors: <http://rsi.aip.org/authors>

## ADVERTISEMENT



Does your research require low temperatures? Contact Janis today.  
Our engineers will assist you in choosing the best system for your application.



10 mK to 800 K  
Cryocoolers  
Dilution Refrigerator Systems  
Micro-manipulated Probe Stations

LHe/LN<sub>2</sub> Cryostats  
Magnet Systems

[sales@janis.com](mailto:sales@janis.com)   [www.janis.com](http://www.janis.com)  
**Click to view our product web page.**

# Nonperturbing electron beam probe to diagnose charged-particle beams

John A. Pasour and Mai T. Ngo

*Mission Research Corporation, Newington, Virginia 22122*

(Received 4 December 1991; accepted for publication 19 January 1992)

A nonperturbing diagnostic tool which is capable of precisely measuring the position and charge distribution of charged-particle beams, including those from rf accelerators, is described. The diagnostic uses as a probe a low-energy (1–20 keV),  $\mu\text{A}$ -level electron beam, which is injected across the path of the primary beam to be diagnosed. The probe electrons are deflected as they pass near or through the primary beam, after which they are collected by a suitable detector. The deflection of the probe electrons depends on the position of the primary beam relative to the test beam as well as on the charge distribution of the primary beam. Consequently, by measuring the deflections, one can determine these primary beam parameters. Calculations which illustrate the capabilities of this technique are presented, and the design and performance of a prototype version of the diagnostic are described. The prototype results agree very well with the calculations, verifying the theory and demonstrating the fundamental soundness of the approach for measuring the position and charge distribution of a relativistic beam. Although the prototype has only been tested with relatively low-energy beams ( $<500$  keV), the extension to highly relativistic beams is straightforward and completely described by the theory. Based on these results, we have a very high degree of confidence that the diagnostic is fully capable of operating as predicted by the calculations.

## I. INTRODUCTION

The successful operation of various high-energy physics experiments, free-electron lasers (FELs), and related devices depends critically on the availability of high-quality and well-diagnosed electron beams. Consequently, there is currently a great deal of interest in the development of diagnostics capable of spatially and temporally resolving various properties of charged particle beams. For example, the short-wavelength FELs now under development at a number of laboratories require very bright electron beams which are positioned to within  $100\ \mu\text{m}$  or less of the wiggler axis. High-energy particle beam colliders require beam positioning to less than  $1\ \mu\text{m}$ . The beams generated by rf accelerators pose particular problems because of their pulse structure. The short ( $<$  tens of ps) duration of the microbunches makes direct real-time measurements difficult or impossible.

Available diagnostics can be divided into two categories: intercepting and nonintercepting. With a highly reproducible or continuous beam, it is possible to insert an intercepting diagnostic (e.g., a wire scanner or thin foil target<sup>1–3</sup>) into the beam to make a measurement and then remove it so that subsequent beam electrons are unperturbed. An example of a state-of-the-art, time-resolved intercepting diagnostic is a quartz Cerenkov radiator, which has been used in combination with a streak camera to measure bunch length with a resolution of  $2.4\ \text{ps}$ .<sup>4</sup> However, a nonintercepting diagnostic is much more desirable in the general case, because it can be monitored continuously and is not subject to damage by the beam. Unfortunately, it is difficult or impossible to measure some quantities with sufficient resolution using available nonintercepting diagnostics.

Nonintercepting diagnostics typically consist of probes

which are sensitive to the electromagnetic fields of the beam. Widely used diagnostics to measure beam current and position are the multiple stripline and button-type wall probes.<sup>5,6</sup> Miniature transmission lines or capacitive probes placed along the beam tube wall are excited by the passing beam, generating a signal proportional to the beam current. Beam position is determined by comparing signals from striplines placed at different azimuthal positions around the tube. Recently, sophisticated signal conditioning, such as heterodyning,<sup>7</sup> has been used to improve the sensitivity and resolution of such detectors. However, these detectors are not sufficiently fast to resolve variations within the microbunch of an rf-linac beam. Furthermore, because the probes are located at the wall of the beam tube, they cannot respond to local asymmetries in the bunch. Therefore, they measure the position of the beam centroid. An rf cavity tuned to the frequency of the accelerator (or its harmonics) also can be used to measure beam current and position. By passing the beam through a square cavity, it is possible to excite modes only when the beam is off center. One implementation of this approach has achieved a spatial resolution of  $\sim 10\ \mu\text{m}$ ,<sup>8</sup> but only on a longer time scale ( $\sim 20\ \text{ns}$ ) and with sensitivity only to the average beam position. A recent variation has used driven chopper cavities to infer bunch length with a resolution of  $\sim 0.2\ \text{ps}$  ( $0.1^\circ$  in phase at  $1.5\ \text{GHz}$ ).<sup>9</sup>

In this paper we describe a diagnostic which has the capability of accurately resolving the position of a charged-particle beam in the beam tube and determining temporal and spatial variations of the beam on the time scale of the microbunch in an rf accelerator. The diagnostic utilizes a probe consisting of a tightly focused, low-energy electron beam, which does not perturb the accelerated electron beam. The basic idea is quite simple, as seen in the schematic diagram of Fig. 1. A tightly focused stream of probe

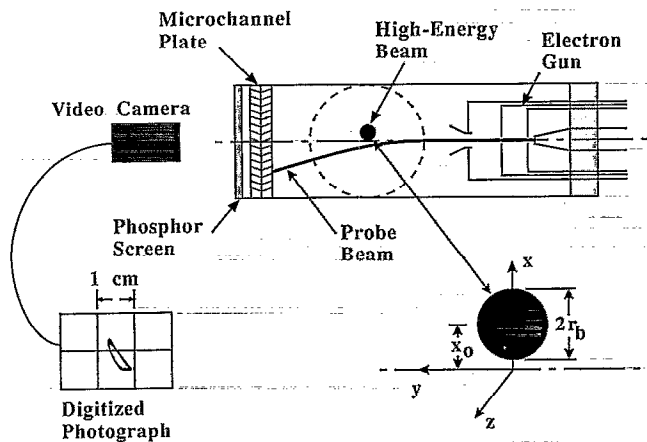


FIG. 1. Schematic diagram of an electron deflection diagnostic, as viewed along the axis of the accelerator beam tube.

electrons is injected across the beam tube perpendicular to the accelerated beam. The probe electrons are deflected by the accelerated beam, and the direction and magnitude of the deflection are directly related to the spatial and temporal charge distribution of the accelerated beam. Electron probes have been used previously to measure plasma sheaths and potentials<sup>10,11</sup> and the neutralization of heavy-ion beams.<sup>12</sup> In the example shown in Fig. 1, a single probe beam is used. However, to determine the absolute position of the beam in the beam tube, two beams 90° apart are required. The deflected electrons impact a detector on the opposite side of the beam tube. In this example, a microchannel plate (MCP) detector is used to collect the electrons and amplify the signal. A phosphor screen on the back side of the MCP produces a light signal which can be photographed to record the deflections. The results of our calculations, which will be summarized below, show that easily resolved deflections are produced by microbunches with total charge as small as a few pCoul and pulse durations as short as 1 ps. The probe electron energy can be adjusted to maximize deflections for a particular microbunch charge. Thus optimized, the diagnostic can determine the position of the microbunch centroid to better than 1  $\mu\text{m}$  with respect to the probe beam. The diagnostic has the capability of time-resolved operation on a picosecond timescale or time-averaged operation with real-time readout, which could be used, for example, by an accelerator operator to tune the beam optics.

This paper is organized into several sections. Section II discusses the theory of the diagnostic. The electromagnetic field from a relativistic beam is calculated and used in a single-particle trajectory code to determine the trajectories of the probe electrons for various beam parameters. The results of this section are used to establish the range of parameters over which the deflection diagnostic can be used to measure the various beam quantities (i.e., position, radius, length, charge per microbunch, and density variations) and the achievable resolution. Section III presents the design details of the complete prototype diagnostic package, including the various components shown in Fig.

1. The results of the experiments we performed with the prototype device are detailed in Sec. IV. Finally, Sec. V summarizes the capabilities of the deflection diagnostic and compares them with those of other available diagnostics. The comparison shows that the deflection diagnostic has some unique capabilities which could be very important in some applications.

## II. THEORY

### A. Fields from the relativistic beam

The electromagnetic fields of a finite electron beam or microbunch can be calculated analytically provided that certain assumptions are made concerning the charge distribution. In all the analytical field calculations performed here, we neglect boundaries. This simplification is justified so long as the beam is propagating along the axis of a long cylindrical tube, as is usually the case in particle accelerators. Furthermore, as we will show in the trajectory calculations below, the probe electron deflection is determined almost entirely by the fields in the immediate vicinity of the microbunch, which are independent of the boundary if it is far away.

We begin by assuming an electron bunch of total charge  $Q$  distributed uniformly in  $r$ ,  $\theta$ , and  $z$  and moving along the  $z$  axis with velocity  $v$ . In the beam frame, the fields are purely electrostatic. For  $r > r_b$ , where  $r_b$  is the microbunch radius, and assuming a bunch length  $L$  in the beam frame, the electrostatic potential is readily found to be (using cgs units)

$$\Phi(r, z) = (Q/\bar{L}) [\ln(\bar{L}/2 - z + u) - \ln(-\bar{L}/2 - z + w)], \quad (1)$$

where

$$u = [r^2 + (\bar{L}/2 - z)^2]^{1/2}, \quad w = [r^2 + (\bar{L}/2 + z)^2]^{1/2}. \quad (2)$$

The electric field is easily obtained from  $E = -\nabla\Phi$ . After transforming the resulting radial and axial electric field components into the laboratory frame (assuming the center of the microbunch is located at the origin of the lab frame at  $t = t = 0$ ), we obtain

$$\begin{aligned} E_r &= \frac{Q}{L\gamma^2} \left( \frac{U}{[(r/\gamma)^2 + U^2]^{1/2}} + \frac{V}{[(r/\gamma)^2 + V^2]^{1/2}} \right) \\ E_z &= \frac{Q}{L\gamma^2} \left( \frac{1}{[(r/\gamma)^2 + U^2]^{1/2}} - \frac{1}{[(r/\gamma)^2 + V^2]^{1/2}} \right) \\ B_\theta &= \beta E_r \\ E_\theta &= B_r = B_z = 0, \end{aligned} \quad (3)$$

where

$$U = L/2 - z + vt, \quad V = L/2 + z - vt. \quad (4)$$

In Eqs. (3) and (4) all quantities are now measured in the laboratory frame, and we have defined the normalized velocity of the accelerated beam to be  $\beta = v/c$  and the normalized energy of the accelerated electrons to be

$\gamma = (1 - \beta^2)^{-1/2}$ . For any charge distribution which is independent of  $\theta$ , Eq. (3) is correct for  $r \gg r_b$ , while the field for  $r < r_b$  is given by replacing  $Q$  with the total charge inside  $r$ .

The field expressions obtained above can be analyzed to gain an insight into the sensitivity of an electron deflection diagnostic to various parameters. One interesting feature is that above a certain energy (typically tens of MeV),  $E_r$  is essentially independent of energy. Also, for high energy,  $E_r$  at a particular observation point varies with time as the axial charge distribution. The axial field approaches positive and negative delta functions corresponding to the head and tail of the bunch. At energies greater than a few MeV, the axial electric field is negligible compared to the radial field. At lower energies, the fields are distributed over a longer time. Just as is the case for a single particle,<sup>13</sup> the time integral of the fields at a particular observation point is independent of energy. (Technically, it is  $\int E v dt$  that is constant, but in all cases of interest  $v \approx c$ .) From this observation it is clear that an electron deflection diagnostic for highly relativistic beams will not be sensitive to beam energy.

## B. Probe electron trajectories

The fields calculated above can easily be used to determine the deflection of the probe electrons. The field components given by Eq. (3) can be substituted directly into the relativistic equation of motion<sup>13</sup> to calculate the electron trajectories. We have numerically solved this equation of motion using a Runge-Kutta algorithm in a relatively simple, three-dimensional trajectory code. We initialize the trajectory code by injecting probe electrons at  $y = -|y_0|$ , as measured from the beam tube axis, with velocity in the  $+y$  direction. The geometry is defined in Fig. 1. Typically,  $y_0$  is in the range from 1 to 7 cm. The position and velocity of a probe electron are calculated for various injection times and for various initial offsets  $x_0$  (defined as the  $x$  displacement between the centroids of the relativistic beam and the undeflected probe beam).

### 1. Effects due to beam offset

To illustrate the nature of the deflection, we plot a series of probe electron trajectories in three dimensions. The trajectories in Fig. 2 are calculated assuming a 200-A, 100-MeV accelerated beam with a length of 0.9 cm (30 ps), moving in the  $+z$  direction inside a 2-cm-diam beam tube. The beam is offset from the axis by 1 mm in the  $-x$  direction. A probe electron is injected into the beam tube every 10 ps, and the trajectories of a number of electrons are plotted as the relativistic beam passes by. The probe electron trajectories are terminated on the wall of the beam tube, and a solid line connects the termination points of successive particles. The maximum deflections are produced when the probe electrons pass closest to the accelerated beam. The degree of deflection can be controlled by varying the beam offset  $x_0$  or the probe beam energy.

To better represent measurements by a detector which could be used in an actual diagnostic device (similar to that shown in Fig. 1), we monitor probe particle location

$I=200$  A,  $\gamma=200$ ,  $\tau=30$  ps,  $r_b=x_0=1$  mm,  $W_0=10$  keV

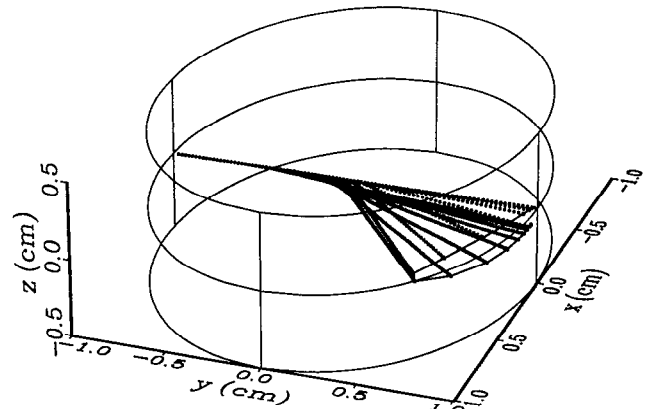


FIG. 2. Three-dimensional probe electron trajectories.

in the  $x$ - $z$  plane at  $y = +1$  cm, corresponding to a detector placed across the beam tube from the injection location. Results from such calculations are shown in Fig. 3 for a primary beam of current  $I = 200$  A and bunch length  $\tau = 30$  ps. In the cases shown here, a probe electron of energy  $W_0 = 10$  keV is emitted every 8.3 ps, ( $c\Delta t = 0.25$  cm), and the points represent the time and position of the electrons when they strike the detector. As above,  $t = 0$  is

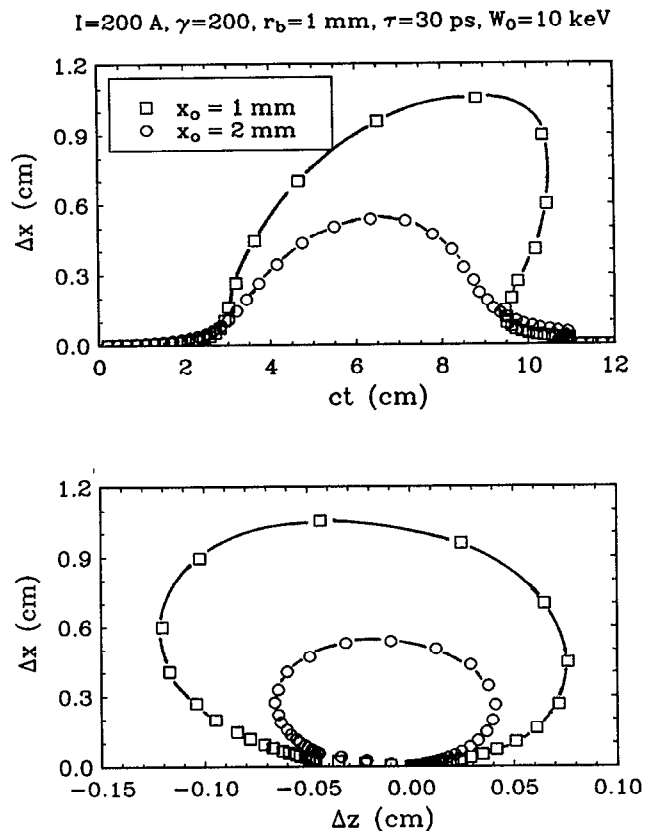


FIG. 3. Deflected electron positions and times at which they reach a planar detector located at  $y = 1$  cm. Points correspond to electrons injected 8.4 ps apart.

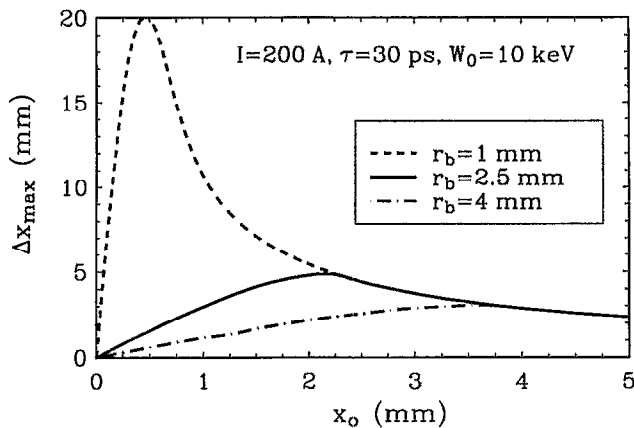


FIG. 4. Maximum transverse displacements vs beam offset for various microbunch radii.

the time at which the center of the bunch passes through the plane  $z = 0$ . Because the probe electrons are accelerated and decelerated by the microbunch and because the deflected electrons travel further than the undeflected ones, the terminal positions of the trajectories can be multivalued in time. The reason for this behavior is easily understood by considering two classes of probe electrons, distinguished by the time they cross the beam tube axis. Particles emitted early in time cross the axis before the microbunch arrives, at which time they are accelerated by the  $y$  component of the electric field. The largest acceleration and deflection are acquired by particles closest to the axis when the bunch passes, which then overtake the earlier electrons. Particles emitted later in time do not cross the axis before the bunch arrives, so they suffer a net deceleration. Again, the electrons closest to the beam tube axis at  $t = 0$  undergo the largest deceleration and deflection. The time required for these electrons to traverse the beam tube and reach the target is longer, resulting in the large displacements observed at late times. Note that the scales for the  $x$  and  $z$  deflections are different. Typically, the  $x$  deflection is much larger than the  $z$  deflection, but when the probe electrons are strongly accelerated and decelerated, the interaction becomes highly nonlinear, and the  $z$  deflection can be quite large.

It is clear from Fig. 3 that the deflected positions of the probe particles are distinguishable if the initial offsets differ, all other quantities being the same. The 1 mm offset electrons pass closer to the primary beam and hence are deflected more than the 2 mm offset electrons. To determine the bunch centroid position, the probe electrons do not have to penetrate the microbunch. However, if the diagnostic is to be used to provide detailed information on pulse shape, bunch length etc., then the electrons do need to penetrate the microbunch, which may require a higher probe beam energy.

## 2. Finite radius effects

The dependence of the probe electron deflection on beam radius is shown in Fig. 4 for a bunch current of 200

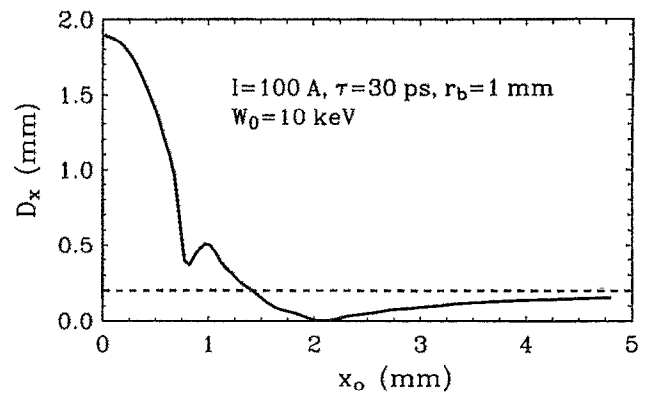


FIG. 5. Probe beam transverse dimension vs offset, illustrating focusing effect.

A and 30 ps length. As expected, there is no dependence if the initial offset is larger than the beam radius. However, if  $x_0 < r_b$ , significant differences are apparent. At the two larger values of beam radius considered (2.5 and 4 mm), the deflections are well behaved, with a gradually increasing amplitude as the offset increases toward  $r_b$ . However, for  $r_b = 1$  mm, the microbunch fields become so large that the probe electrons are slowed drastically (and nearly reflect) when  $x_0 < r_b$ . This results in a very nonlinear interaction, greatly increasing the sensitivity of the diagnostic. In general, maximum sensitivity to the position of the microbunch is obtained by using the lowest possible probe electron energy consistent with generating deflections which fall within the acceptance range of the detector.

Figure 4 shows that the maximum deflection of the probe electrons increases with beam offset until the offset is on the order of the microbunch radius. Further increasing the offset from that point leads to a gradual decrease in the maximum deflection. This trend is very general. One practical implication of this effect is that an absolute determination of beam position from a measurement of the maximum probe-particle deflection is not possible unless several measurements are made with different offsets or unless one is certain that the offset is either large or small compared with the bunch radius. In most cases, this will not be a serious limitation because either the diagnostic configuration can be chosen so that it is known *a priori* that  $x_0 > r_b$ , or the diagnostic can be used interactively with the beam transport optics so that the degree of offset becomes clear based on changes in the deflection as the optics are tuned.

There is also a focusing effect, which can be quite pronounced for a finite-radius probe beam, that might also be used to determine the relative displacement of the probe beam and the high-energy beam. If  $x_0 > r_b$ , the fields of the energetic beam are radially decreasing, which tends to focus the probe electrons in the  $x$  direction. If the probe beam passes near the center of the energetic beam, the fields are increasing with  $r$  and strongly defocusing. This effect is illustrated in Fig. 5, in which the  $x$  dimension of the probe beam is plotted versus the offset between the centers of the two beams. We have assumed a unidirectional probe beam having a diameter of 0.2 mm, denoted

by the dashed line, and the measurement is made at  $y = 1$  cm. The notch in the curve at  $x_0 = 0.8$  mm corresponds to the peak deflection, which is relatively sharp for these parameters. The detailed shape of this curve is quite sensitive to the probe electron energy, at least in the nonlinear regime. Nevertheless, it is clear that this focusing effect could provide a sensitive method for determining the centering of the energetic beam as well as an approximate indication of its radius.

### 3. Effects due to nonuniformities

One of the unique and intriguing features of the electron deflection diagnostic is its potential for resolving at least some of the microstructure of the accelerated beam. The field profiles of nonuniform charge distributions can be substantially different from those of uniform beams. To determine the degree to which the deflection diagnostic can resolve such differences, we have modified the trajectory code to incorporate specific types of beam nonuniformities. Purely radial or axial density variations are easily treated by simply multiplying the uniform-density field values by the appropriate shape factor. Azimuthal variations require a more difficult integration which generally cannot be performed analytically. For our present purposes, it has been more expedient to model azimuthal nonuniformities by using multiple beamlets of different uniform charge density to make up the microbunch.

We first consider the effect of microbunch length. Fixing the charge per bunch at 10 nC, we perform calculations with bunch length varying from 30 to 300 ps. Figure 6 shows the transverse and axial displacements of probe electrons having energies of 10 keV. In each case the displacements are measured in an  $x$ - $z$  plane located at  $y = 1$  cm. The plotted points correspond to electrons injected at 8.3 ps intervals. It is clear that the magnitude of the electron deflection is very sensitive to bunch duration. However, it is important to note that in the cases shown here, the deflection is in the nonlinear regime. If the energetic beam current is too low to decelerate and accelerate the probe electrons appreciably, the deflection is nearly constant for a particular charge per bunch, independent of the bunch length. The probe electron energy must be chosen with this in mind. By properly choosing the probe beam energy, it is possible to resolve the bunch duration to within a few percent if the charge per bunch is known.

Two regimes are apparent in Fig. 6. For the shorter bunch lengths (and/or a low-energy probe beam), the magnitude of the deflection varies rapidly with bunch length, but the time during which electrons are deflected from their initial position is essentially independent of bunch length. In this regime, the charge per bunch must be known independently if this diagnostic is to be used to measure the bunch length quantitatively, because a larger charge can produce the same deflection magnitude as a shorter duration bunch. In the second regime, both the amplitude of the deflection and the time during which electrons are deflected vary with bunch length. This regime is characterized by relatively long bunch lengths and/or a high-energy probe beam, which produce nearly constant-

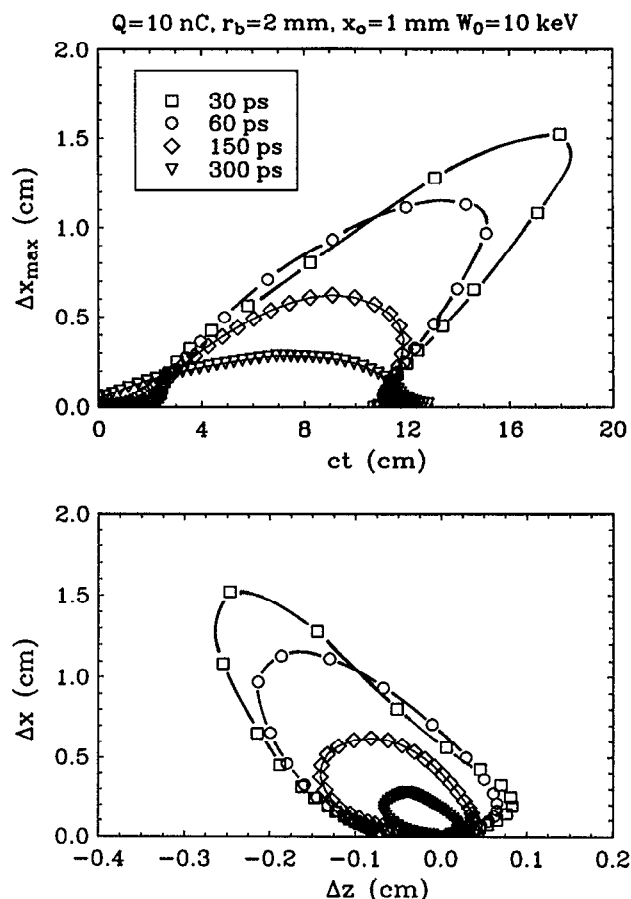


FIG. 6. Transverse and axial deflections of 10 keV probe electrons, as measured at  $y = 1$  cm, for various microbunch lengths.

amplitude deflections for the duration of the microbunch. In this regime, both the pulse duration and the charge per bunch can be unambiguously determined by the deflection diagnostic if the bunch radius and the relative injection position  $x_0$  are known. If the probe beam can be scanned in a controlled manner across the microbunch, it is possible to determine the bunch radius as well as its position in the beam tube. Thus, in principle, this single diagnostic can determine bunch radius, length, charge, and position. However, to perform all these measurements, the electron detector must be able to resolve the duration of the deflection, which is essentially the bunch duration in the second operating regime. Although this requirement is a stringent one given a microbunch duration of tens of ps, high-speed streak cameras are available which could be used for this purpose in many cases. It is also possible to sweep the probe electrons in the  $z$  direction to obtain temporal resolution.

Variations in radial profile can also be treated. Two particular profiles are considered here, one peaked on axis and the other peaked near the edge. The charge-density profiles and the corresponding radial electric field profiles are shown in the upper graphs of Fig. 7. For comparison, the profiles are normalized to the uniform density case, which is also shown. The total charge in each case is iden-

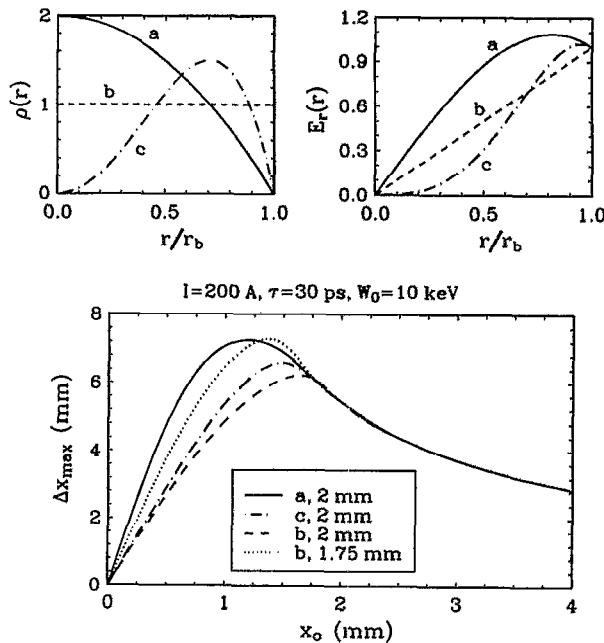


FIG. 7. Top: radial density profiles (left) and corresponding  $E_r$  profiles. Bottom: maximum deflection (at  $y = 1$  cm) vs offset for different radial profiles and  $r_b = 2$  or  $1.75$  mm.

tical. The peaked distribution varies as  $1 - (r/r_b)^2$ , and the annular distribution varies as  $(r/r_b)^2 - (r/r_b)^4$ . The deflections produced by these types of beams are shown in the lower graph of Fig. 7. The results indicate that there is a measurable difference in deflection for the various radial profiles, with the largest difference produced by the profile which is peaked on axis. As they must, all profiles produce identical deflections when  $x_0 \geq r_b$ . One might expect the annular profile to produce a smaller deflection for small  $x_0$  than is shown in the figure. The reason this is not the case is that most of the deflection in both the uniform and annular beam cases occurs as the probe particle passes near the outer edge of the beam, even at small  $x_0$ . As shown in the figure,  $E_r$  is actually smallest in this region for the uniform beam.

From the results of these calculations, it is clear that the electron deflection is quite sensitive to radial profile if the beam radius is known. In practice, however, it is more difficult to distinguish between a uniform beam and a larger diameter beam with a density peaked on axis. The dotted curve in Fig. 7 demonstrates this point. A uniform beam has been chosen with a radius which gives the same maximum deflection as the peaked distribution. Even in this case, there is a measurable difference between the two curves. However, it is obvious that simply determining the maximum deflection that can be achieved from a given beam is not enough to determine the radial or axial profile. Only by making a series of measurements at various values of  $x_0$ , and possibly at different electron energies, would it be possible to determine these profiles quantitatively. The results of the measurements would have to be compared to values computed using different assumed profiles, bunch

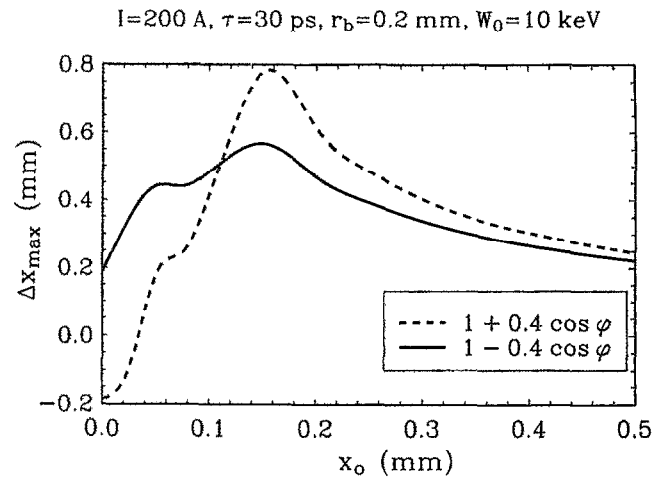


FIG. 8. Maximum deflection vs offset of the geometric center of a microbunch with two azimuthally asymmetric charge distributions.

length, and bunch radius in order to arrive at a true bunch profile. The more that is independently known about the beam, the simpler this comparison will be.

To determine the effect of an azimuthal charge variation, we assume a microbunch in which the charge is displaced toward one side. Figure 8 shows the maximum deflections as a function of offset of the geometric center of the microbunch for a 40% enhancement of charge density in the  $+x$  and  $-x$  directions. Here, the bunch is annular (inner radius  $= 0.44r_b$ ) and is comprised of uniform beamlets arranged in a  $\cos \varphi$  distribution. Again, the measurements are made at  $y = 1$  cm. There is a clear asymmetry in the deflections. By making measurements at multiple values of  $x_0$ , it is possible to quantify the deflection asymmetry and deduce the degree of charge asymmetry which is responsible. In practice, such a measurement would probably require the probe beam to be scanned over the cross section of the microbunch. It might be quite difficult to obtain a precise mapping of the charge density, but a general picture of the degree and direction of the asymmetry is well within the capability of the diagnostic.

#### 4. Example

As a final numerical example, we consider the use of the deflection diagnostic with a tightly focused, ultrarelativistic beam. Although the beam energy (50 GeV) is much higher than considered in the previous cases, we noted above that the deflection diagnostic is independent of energy for highly relativistic beams, so we would not expect the high energy to be important. The results of trajectory calculations for this beam are plotted in Fig. 9. The maximum deflection agrees to three significant figures with the deflection from an otherwise identical 100 MeV beam. The general behavior is the same as described previously. However, the more tightly bunched beam requires a higher probe beam energy to penetrate the Coulomb barrier.

For offsets less than  $20 \mu\text{m}$ , the 20 keV probe electrons in Fig. 9 are displaced more than  $1.2$  mm for each  $\mu\text{m}$  of beam offset. These measurements are made at a distance



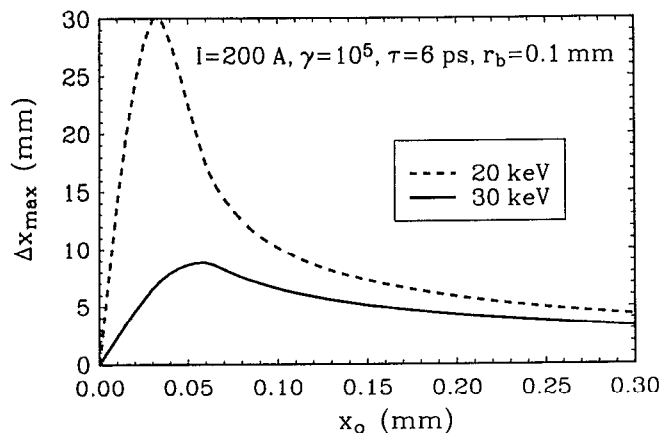


FIG. 9. Maximum deflection of 20 and 30 keV probe electrons vs offset for a tightly focused, ultrarelativistic beam.

$y = 1$  cm from the tube axis, so the largest deflection observed corresponds to an angular deflection of over  $70^\circ$ . This deflection is somewhat too large for simple detector configurations, especially if the beam tube diameter is much larger than 2 cm. However, at a probe electron energy of 30 keV, the maximum deflection is acceptable up to a beam tube diameter of about 5–10 cm. (The limitation here is the active area of available electron detectors.) The ability to adjust the probe electron energy to optimize deflections (maximize sensitivity) is an important advantage of this diagnostic. In particular, this example suggests an operating procedure whereby a relatively high probe energy is used until the deflection (and hence the relative beam offset) is very small. Then decreasing the probe energy allows the resolution of the diagnostic to be increased to  $1 \mu\text{m}$  or less. In general, deflections on the order of the probe beam diameter or detector resolution can be measured. This deflection resolution can be as small as  $10 \mu\text{m}$ , which corresponds to an offset resolution of about 10 nm in this example. Of course, this resolution is relative rather than absolute unless the absolute position of the probe beam is known. The definition of an absolute reference point then becomes crucial.

For even more tightly bunched beams, such as in particle colliders, the probe electron energy required to penetrate the Coulomb potential can become quite large. In such cases, it would be more feasible to use an ion probe beam. Such a beam (22 keV  $\text{He}^+$ ,  $0.1 \mu\text{A}$ , 0.5 mm diameter) has been used to probe rapidly varying fields in plasmas.<sup>14</sup> Much more tightly focused ion beams are now available.<sup>15</sup>

### III. EXPERIMENTAL SETUP

The development and testing of the electron deflection diagnostic were performed using the apparatus shown in Fig. 10. The system was evacuated to a typical vacuum level of  $10^{-5}$ – $10^{-6}$  Torr by two turbomolecular pumps, one stationed at the diode section and the other at the diagnostic section. The major components in this arrangement are the electron beam generator for the main beam

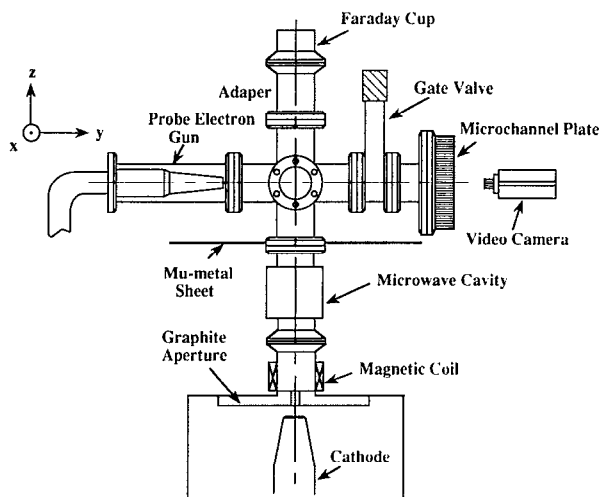


FIG. 10. Schematic diagram of the prototype electron deflection diagnostic.

(the beam being diagnosed), a microwave cavity to modulate the main beam, the probe electron gun, and the detector for monitoring the deflected electrons. These components are described below.

The main electron beam used to test the diagnostic was generated by two different pulsed power devices. The first one, a modulator consisting of a PFN and a step-up pulse transformer, produced a voltage pulse ranging from 60 to 200 kV with a 500 ns duration. The second one was a Febetron, a Marx-type generator which produced a 50 ns pulse at a moderately higher voltage (200–600 kV). Most of the kA-level current from the Febetron was shunted by a high-power  $\text{CuSO}_4$  resistor in parallel with the diode. The electron beam from both of these generators was field emitted from velvet covered cathodes. Beam current and size were limited to the desired values by apertures with various diameters. For the available range of main and probe beam energy and the size and location of the electron detector, it was predicted from the numerical calculations described in the previous section that the main beam current should be on the order of 100's of mA (no greater than 1 A). The restriction on the beam current is necessary to keep the amplitude of the deflection within the detector field of view.

The original motivation for this diagnostic was for rf accelerators. However, due to the shutdown of the NIST racetrack microtron at which we had planned to test the diagnostic, we were forced to improvise by using a modulated, low-energy beam. Although there are substantial differences in the expected behavior of the diagnostic at these low energies versus the ultrarelativistic beams that can be generated with rf accelerators, these tests allowed us to test the operation of the diagnostic with short electron bunches ( $\leq 100$  ps). In our experiments, the electron beam was passed through an rf cavity, which was driven by a high-power microwave pulse at  $\sim 3$  GHz. The input and output apertures of the cavity were 1.5 mm in diameter. The  $\text{TE}_{101}$  mode cavity was loop excited from a coaxial transmission



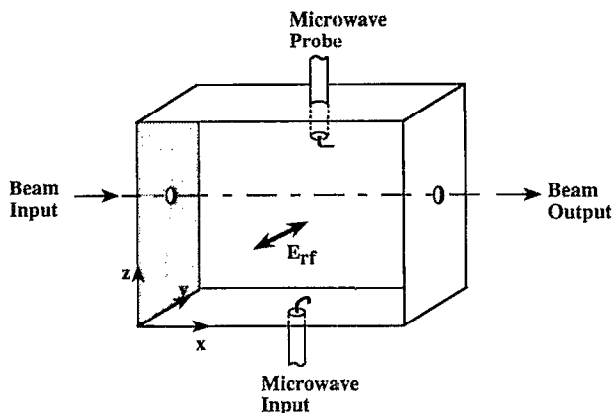


FIG. 11. rf cavity used to modulate the main electron beam.

line. The beam was consequently modulated by the rf field, as shown in Fig. 11. The cavity was fabricated from a 7-cm-long section of an S-band waveguide, and the  $Q$  was measured under vacuum and in the absence of the beam to be about 550. The input rf power was generated by a tunable, 1- $\mu$ s pulse width, 0.1–1 MW magnetron. Using a high-power attenuator, the microwave power could be adjusted down to a few tens of kW. The peak-to-peak deflection of the electrons was calculated to be  $\Delta y = 0.4P^{1/2}$  mm, where  $P$  is the input power in kW. With the TE mode cavity, the beam emerges from the cavity with no velocity modulation.

A low-cost CRT-type electron gun was chosen for the probe electron beam, which intersected the accelerated electron beam near the center of a five-way vacuum cross. The electron energy and the emitted current of the gun could be varied from 0 to 10 keV and up to several hundred nA, respectively. Due to imperfections in the probe electron gun and the relatively long distance from the gun to the microchannel plate (26 cm), the beam was almost 1 mm in diameter at the microchannel plate. The position of the probe electron beam could also be controlled by adjusting the bias voltage applied to the horizontal and vertical deflection plates of the gun.

The electron detector used in these experiments was a 4-cm-diam microchannel plate (MCP) from Galileo Electro-Optics Corporation.<sup>16</sup> The chevron-type MCP had a resolution (as determined by channel diameter and spacing) of  $\sim 20 \mu\text{m}$  and a maximum gain on the order of  $10^8$ . The electrons emerging from the MCP were accelerated to an integral phosphor screen. With this arrangement the MCP was capable of detecting single electrons, allowing electron deflection to be detected on a picosecond time-scale. Deflection of the probe electrons was monitored by a high-sensitivity CCD video camera and recorded on a video cassette recorder for further measurements and data analysis. Typical dc operating voltages for maximum MCP sensitivity were  $(V_o - V_i) = 2 \text{ kV}$  and  $(V_s - V_o) = 5 \text{ kV}$ , where  $V_o$ ,  $V_i$ , and  $V_s$  are the output plate and input plate voltage of the MCP and the phosphor screen voltage, respectively.

The major problem that had to be overcome before the

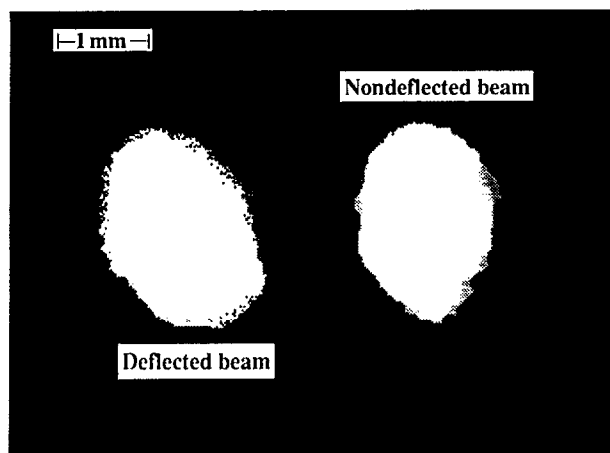
MCP could be used efficiently was the unacceptably low signal-to-noise ratio. An extremely large MCP output was produced when the main electron beam was fired, completely masking the image from the deflected probe electrons. Because a MCP is sensitive to both charged particles and x rays, the noise arose from several sources, including stray and scattered primary beam electrons, secondary electrons or bremsstrahlung x rays emitted when the primary electrons struck the walls of the vacuum tube, or plasma generated by electron collisions with the background gas in the system or with the surfaces.

Several techniques were used to improve the signal-to-noise ratio. The largest noise reduction was achieved by gating the high-voltage pulse applied to the MCP. The gate pulse was generated by a hard-tube pulser, which we built using two krytron switches. A capacitor was discharged across the MCP by the first krytron switch and then crowbarred by the second krytron after the desired delay time (pulse width). With this generator, the pulse duration could be varied from 0.5 to 1.2  $\mu\text{s}$ , and the output voltage could be adjusted from 0.8 to 3 kV. To achieve the maximum noise reduction from the gated MCP, the main beam generator was synchronized to fire at the end of the gate pulse, thereby minimizing the time any secondary or plasma electrons could activate the MCP. Additional noise reduction measures included wrapping lead around the MCP and the beam tube, baffling the probe electron gun to prevent stray electrons from reaching the MCP, and biasing the MCP to repel low-energy electrons ( $\leq 500 \text{ eV}$ ).

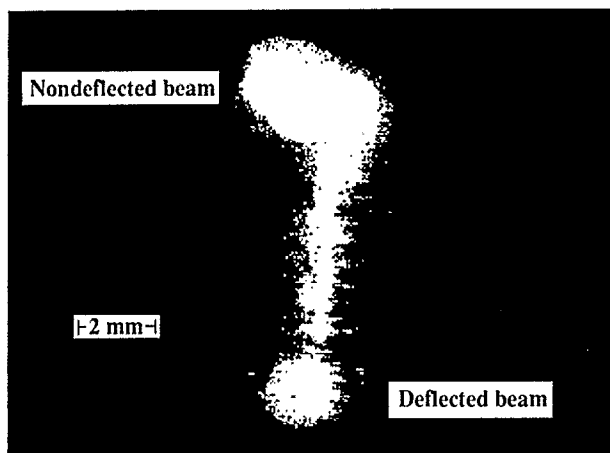
During the testing, parameters such as position of the main beam relative to the vacuum tube, beam diameter, and charge density profile of two different long-pulse beams and a modulated beam were diagnosed. This was accomplished by measuring the probe electron deflection as a function of probe beam energy and relative offset for various main beam voltages and currents. To the extent possible, the main beam parameters were determined independently to verify the performance of the diagnostic. The main beam current was measured using a Faraday cup, and the time-integrated beam size and position were determined from a scintillator target placed in the center of the five way cross (and removed prior to using the probe beam). Main beam energy was obtained by a capacitive voltage divider at the output of the modulator. The location of the probe beam at the center of the cross was precisely determined by scanning a wire across its path with a micrometer-drive positioner. Repeating this procedure for a number of probe beam injection angles while simultaneously monitoring the image on the MCP provided a calibration of absolute probe beam position at the interaction point as a function of image position.

#### IV. EXPERIMENTAL RESULTS

The experimental results have verified most of the important features of the electron beam deflection diagnostic, although there were numerous constraints in the experimental setup and a limited range of parameters of the main beam. Nevertheless, the experimental data were very reproducible and agreed extremely well with the theoretical



(a)



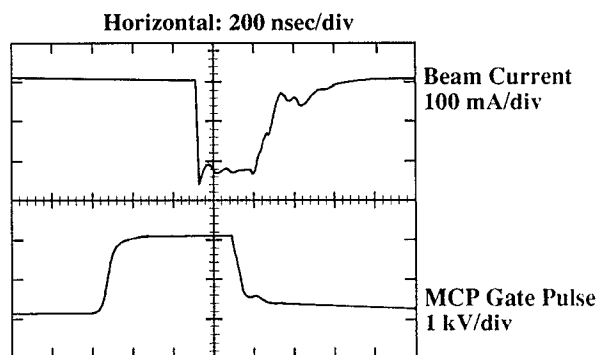
(b)

FIG. 12. Images of electron deflections by (a) a 500 ns electron beam and (b) a 50 ns electron beam.

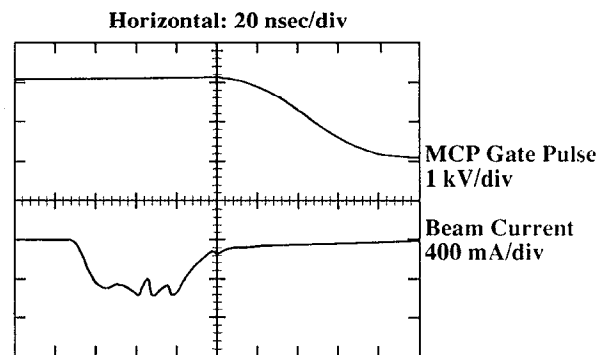
calculations. The experimental results will be divided into two sections by the characteristics of the beam to be diagnosed: (a) long electron beam pulses, i.e., 500- and 50 ns, and (b) a modulated beam at 3 GHz.

#### A. Long electron beam pulses

The diagnostic was first tested using the two electron beams described in the previous section. The deflection of the probe electron beam as recorded by the MCP is shown in Fig. 12 for the two main beam durations. The two white spots in Fig. 12(a) correspond to the nondeflected beam (right), and the deflected beam (left). In this image the main electron beam is on the right, traveling vertically upward. The probe beam energy  $W_0$  was 2.57 keV and the beam offset  $x_0$  was 0.62 cm. Figure 12(b) shows the deflection of the probe electrons due to the 50 ns main beam. This result was obtained with  $W_0 = 1.3$  keV and  $x_0 = 0.3$  cm. In Fig. 12(b) the main electron beam was on the top and traveling from left to right. The probe electron beam



(a)



(b)

FIG. 13. Relative timing between the main beam current pulse and the MCP gate pulse. (a) 500 ns beam and (b) 50 ns beam.

deflected from top to bottom as the main beam current increased from zero to maximum, remained almost at the same place during the flat portion of the pulse, and went back to the original position as the current decayed to zero. The rise and fall times of about 8 and 10 ns, respectively, of the main current pulse produced the vertical streak between the two end points. Qualitatively, the deflection behaved as expected, reversing directions when the probe beam was scanned to the opposite side of the main beam and increasing in magnitude as  $x_0$  approached  $r_b$ . As the main beam pulse duration decreased, the MCP gain had to be increased, resulting in some blooming of the undeflected electron image. Figure 13 shows the relative timing between the main beam current for the 500- and 50- ns beams and the MCP gate pulse. Notice that in both cases the current pulse occurred near the end of the MCP gate pulse.

Measurements of the probe electron deflection as a function of main beam current are shown in Fig. 14, along with the theoretical calculation. The main beam energy in this case was 65 keV, with a beam radius of 0.3 cm. The probe beam energy was 2.3 keV, with an offset of 0.26 cm from the main beam center. As predicted from the trajectory code, the electron deflection increases linearly with main beam current. In this linear regime, the main beam current is small enough that there is no appreciable deceleration or acceleration of the probe electrons. To keep the deflection within the active area of the MCP with a higher current beam, it would be necessary to increase the probe

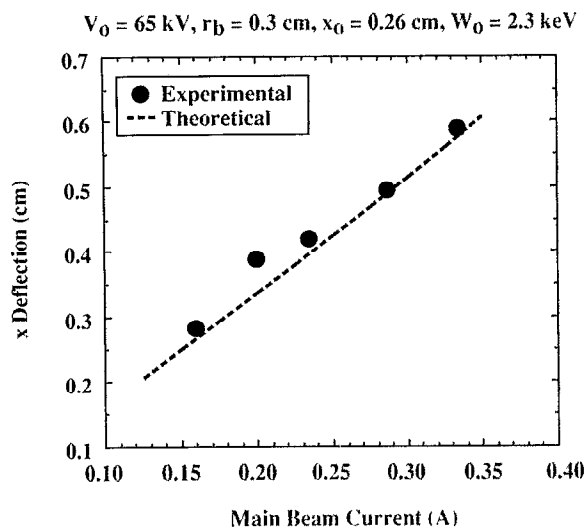


FIG. 14. Transverse ( $x$ ) deflection vs main beam current.

beam energy, decrease the offset, or decrease the distance to the MCP.

Figure 15 shows the experimental and theoretical dependence of the probe electron deflection on the probe beam energy for the two main beam pulse durations. Due to the shot-to-shot amplitude variation in the main current pulse ( $\sim 10\%$ ), the normalized electron deflection (i.e., deflection to main beam current ratio) is plotted in this and the remaining figures. From Fig. 14, it is clear that for the ranges of probe beam energy and main beam current that we have used, the normalized deflection is constant as a function of the main beam current. This, however, is not the case for low probe electron beam energy (i.e.,  $< 1$  keV). The symbols and error bars in the figure represent the average and the range of deflections measured over

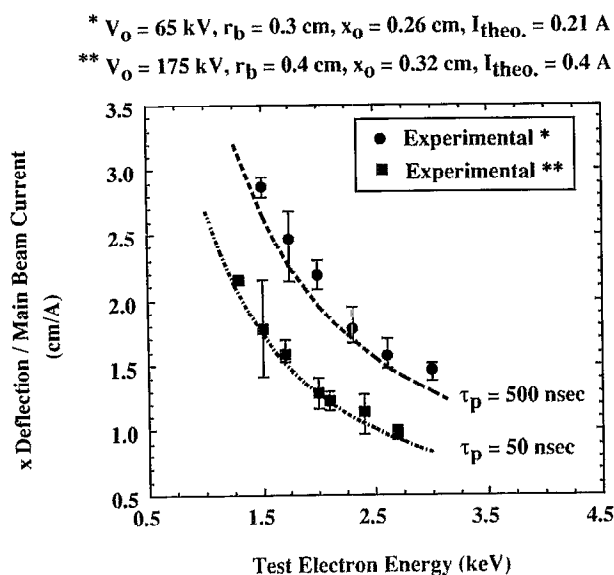


FIG. 15. Normalized electron deflection vs test beam energy for long-duration beams.

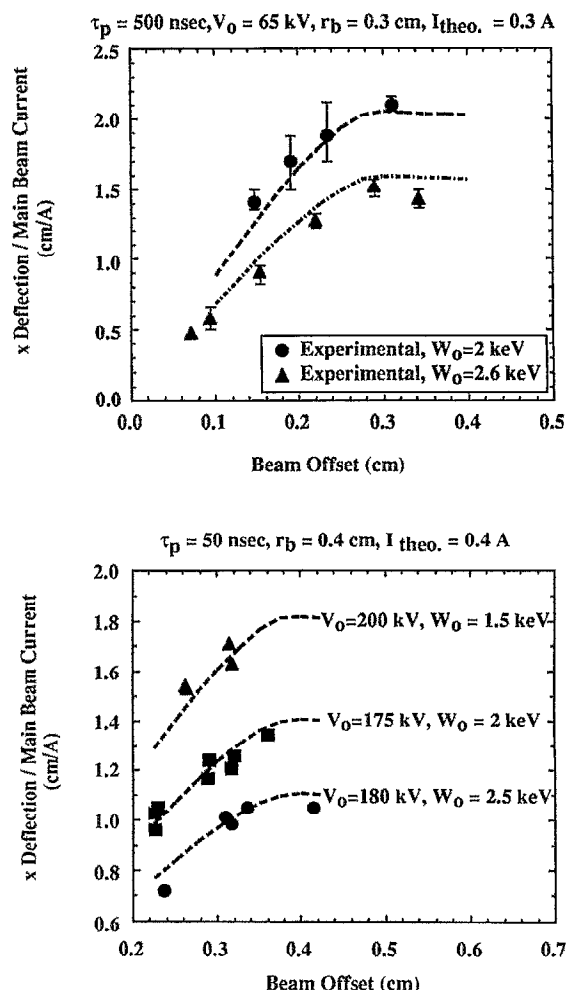


FIG. 16. Normalized electron deflection vs beam offset. Top: 500 ns beam. Bottom: 50 ns beam.

several shots. The experimental data agree very well with the predicted deflections. The slight discrepancies can be explained by the small uncertainties in the calibrations of the main electron beam diagnostics (i.e., Faraday cup and capacitive voltage divider), uncertainty in determining the main beam current and voltage (which vary during the pulse), and by uncertainty in measuring the amplitude of the deflection.

The rapid decrease in deflection amplitude with increasing probe beam energy results from two effects. First, lower-energy electrons interact with the main beam for a longer time, thereby acquiring a larger transverse velocity  $v_x$ . Second, the lower-energy (lower  $v_y$ ) electrons take longer to reach the MCP, so their deflection would be larger even if  $v_x$  were the same. Combining the effects, the deflection angle  $v_x/v_y$  then is much larger for lower-energy probe electrons.

To determine the dependence of the deflection on beam offset, the probe beam was scanned across the main beam. Sample experimental deflections are shown in Fig. 16 along with the theoretical calculations for different probe electron beam energies. The deflection of the probe electron

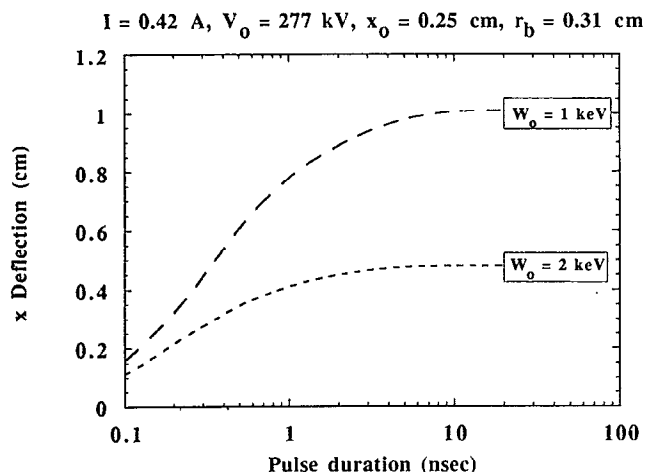


FIG. 17. Theoretical  $x$  deflection vs pulse duration.

beam increased linearly with beam offset until the offset was on the order of the main beam radius. (Theory predicts a slow decrease for further increases in beam offset, but the limited size of the MCP and the large distance from the interaction point to the detector limited the maximum offset in the experiment.) Similar behavior was observed for all probe beam energies and both main electron beams, and as expected, higher deflection was obtained with lower probe beam energy. This result demonstrates that by measuring probe beam deflection as a function of beam offset, the size and position of the main beam can be determined. However, to fully resolve the beam size and position, several measurements have to be made at various offsets.

It is worthwhile to point out that the electron deflection is independent of the pulse duration of the main beam for pulses greater than a few nanoseconds. As shown from the experimental results, the electron deflection exhibits similar behavior for both the 50 and 500 ns pulse durations. However, the deflection varies drastically with pulse duration for pulses on the order of a few nanoseconds or less. The trajectory calculations demonstrating this point are shown in Fig. 17. The reason for this behavior is that for a given probe electron beam energy, there is a finite interaction region over which the probe electrons experience the fields of the main electron beam. When the main beam length is shorter than this interaction region, the impulse given to a probe electron is smaller than it is from a longer beam of the same current. However, once the main beam is longer than the interaction region, the impulse is independent of bunch length, because only that portion of the main beam inside the interaction region contributes to the deflection.

## B. Modulated electron beam

The final tests of the diagnostic were performed by modulating the Febetron beam at 3 GHz, thereby simulating an rf linac type beam, using the setup shown in Fig. 10. These experiments were the only ones to use the magnetic field coil shown in this figure. The field was required because of the increased distance over which the main beam

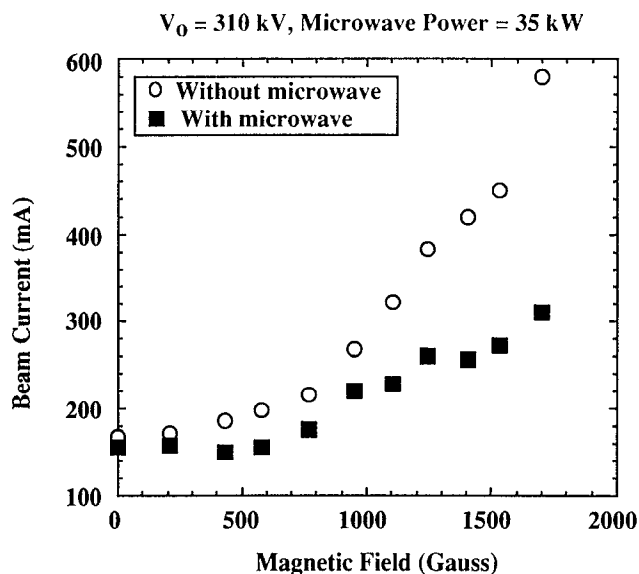


FIG. 18. Average beam current vs magnetic field with and without microwave modulation.

had to be transported with the modulation cavity in place. Figure 18 shows the main beam current with and without microwaves as a function of magnetic field for a constant beam voltage and microwave power. The beam current generally increased with magnetic field, but the increase was much less with the modulation. This behavior is explained by the fact that at low magnetic field, the main beam expanded considerably as it passed through the cavity. The beam radius at the output aperture was larger than the amplitude of the deflection produced by the rf field, so no change in current was observed. At higher magnetic field, the beam was smaller than the amplitude of the deflection, and the beam was swept back and forth across the aperture, resulting in a strong modulation of the beam emerging from the cavity. Thus, although the average beam current measured with the Faraday cup was reduced to about half the value without the microwaves, the peak current of the bunches should have remained about the same.

An example of the deflection produced by the modulated beam is shown in Fig. 19. The image of the deflected electrons is much fainter and often more smeared out than with the unmodulated beam. Qualitatively, this is expected due to the rapid oscillation of the probe electrons being deflected by the individual beam bunches. To quantify this behavior, the particle trajectory code was modified to include a train of five identical beam bunches spaced at an interval of 333 ps (3 GHz). (Five bunches were thought to be sufficient because their total spatial extent is approximately the same as the interaction region of any single-probe electron.) The calculations showed that the deflection due to the train of bunches was  $\sim 25\%$  larger than that due to a single bunch, and the oscillation amplitude ranged from 10% to 30% of the total deflection for parameters pertinent to our experiment. These calculations revealed a shortcoming in the use of the modulated low-

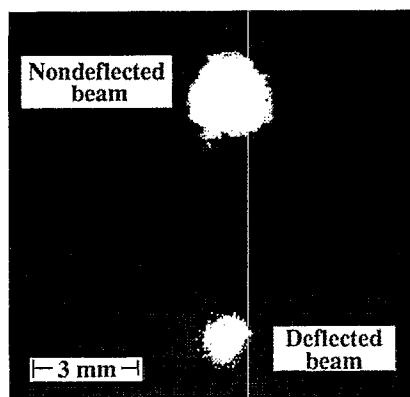


FIG. 19. Image of probe electron deflection by a modulated electron beam.

energy beam to simulate an rf linac beam—the deflection amplitude for our parameters is not very sensitive to the bunch length. This differs from the high-energy case, which we described in Sec. II (see Fig. 6). Nonetheless, these calculations allowed us to make quantitative comparisons of the experimental results and the theory, thereby verifying the performance of the diagnostic with an rf modulated beam.

Figure 20 shows a comparison of the experimentally measured deflections with the calculated values for different probe beam energies. The best fit to the experimental data was obtained using the parameters shown in the figure. The measured values of  $x_0$  and of the main beam energy (275 keV) and average current (0.4 A) were used in the calculations. The best-fit beam radius (0.25 cm) was less than the measured value of 0.3 cm, possibly indicating that the current distribution was peaked on axis. The

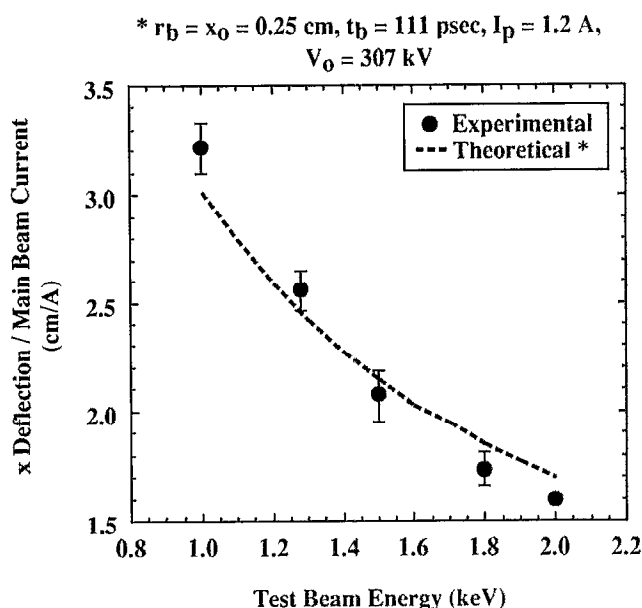


FIG. 20. Normalized electron deflection vs test beam energy for a modulated beam.

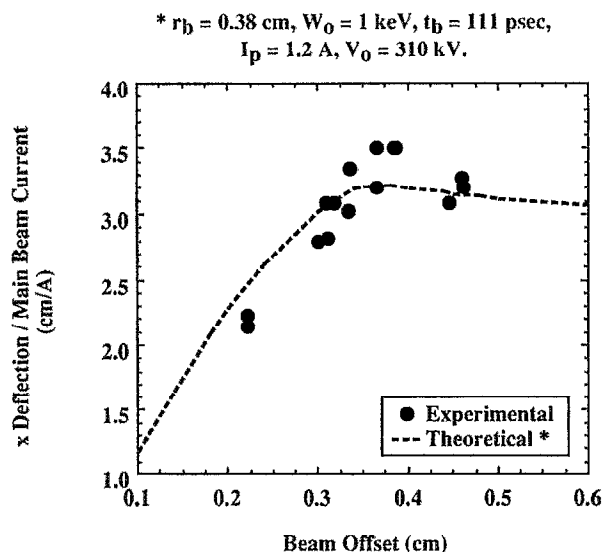


FIG. 21. Normalized electron deflection vs beam offset for a modulated beam.

bunch duration of one third of the rf period and peak current of 1.2 A are certainly plausible.

The experimental variation in deflection with beam offset is compared to theory in Fig. 21. Each of the experimental data points represents a single shot, and the scatter is representative of the uncertainty in measuring the deflection and the variation of current during the pulse (the average value of which is used to normalize the data). The range over which the offset could be varied was limited by the experimental apparatus, but over the accessible region, the agreement with theory is quite good. The beam radius that is inferred from the diagnostic by the point of maximum deflection is 0.38 cm, while the target/scintillator measurement gave 0.40 cm in this case. The good agreement between the experiment and calculations indicates the suitability of the beam deflection diagnostic for bunched beams.

## V. DISCUSSION

The basic idea of the electron deflection diagnostic is quite simple, but the prototype development revealed a number of difficult detection problems that had to be overcome to achieve a sufficient signal-to-noise ratio. The intrinsic detection problem which must be faced is the small number of deflected electrons that are available for detection when the diagnostic is used with an rf-accelerated beam. If the probe beam current is  $1 \mu\text{A}$  (which is quite high for a high-quality, tightly focused beam), there are only six electrons per ps available for detection. Detection of such a small number of electrons requires a very quiet background and a high detector sensitivity. The MCP used in the prototype has ample sensitivity to respond to single electrons, but it also responds to x rays and to any stray charged particles. These extraneous sources must be almost totally eliminated, at least for the time that the detector is active, in order to be able to achieve ps response.

A second issue which must be addressed is the density of the relativistic beam to be diagnosed. If the beam is tightly focused and bunched (as in a particle collider), an energetic probe electron beam is required to penetrate the Coulomb barrier of the bunch if the diagnostic is to be used to resolve the charge distribution of the bunch. However, it is important to note that the position of even a tightly focused bunch can be accurately determined with this diagnostic without the probe electrons actually penetrating the bunch.

Compared to other available diagnostics, the electron deflection diagnostic has some obvious advantages. The resolution with which it can measure position is as good or better than most other diagnostics, perturbing or nonperturbing. As we have shown, the position resolution can be on the order of microns or less with suitably chosen parameters. Because it employs a stream of particles which can penetrate the accelerated beam, the deflection diagnostic also has the ability to resolve the microstructure of the beam. Based on the calculations presented in Sec. II for several specific cases, the diagnostic can resolve bunch length to within about 10% or a few ps, bunch radius to within 10%, and radial, axial and azimuthal density variations which significantly deviate from uniform density. Obviously, the precision with which any of these quantities can be measured in a particular accelerator depends on the beam parameters, the availability of independent beam data (e.g., average current), and on the complexity of the deflection diagnostic. None of the other nonperturbing diagnostics which have been developed have the ability to resolve beam microstructure, and no other single diagnostic has the ability to measure as many of the beam parameters as this one. The major disadvantages of the deflection diagnostic are its complexity, cost, and the somewhat involved computations that are required to analyze the data. When viewed in the context of a large accelerator facility,

however, these disadvantages are not too significant.

## ACKNOWLEDGMENTS

The authors wish to thank Dr. Steven Gold of the Naval Research Laboratory for the loan of the Febetron used in these experiments. The expert assistance of Mr. Allen Kinkead and Mr. Mark Sucy in the fabrication and operation of various components is also gratefully acknowledged. This work was supported by the U. S. Department of Energy, under Contract No. DE-AC05-88ER80628.

<sup>1</sup>L. Wartski, S. Roland, J. Lasalle, M. Bolore, and G. Filippi, *J. Appl. Phys.* **46**, 3644 (1975).

<sup>2</sup>X. K. Maruyama, J. R. Neighbours, and F. R. Buskirk, *IEEE Trans. Nucl. Sci.* **NS-32**, 1994 (1985).

<sup>3</sup>M. Ross, in *Accelerator Instrumentation, Second Annual Workshop*, AIP Conf. Proc. No. 229, edited by E. S. McCrory (AIP, New York, 1991), pp. 88–106.

<sup>4</sup>J. C. Sheppard, J. E. Clendenin, M. B. James, R. H. Miller, and M. C. Ross, *IEEE Trans. Nucl. Sci.* **NS-32**, 2006 (1985).

<sup>5</sup>R. Talman, in *Accelerator Instrumentation*, AIP Conf. Proc. No. 212, edited by E. R. Beadle and V. J. Castillo (AIP, New York, 1991), pp. 1–25.

<sup>6</sup>R. E. Shafer, in Ref. 5, pp. 26–58.

<sup>7</sup>R. Webber, J. Fritz, S. Holmes, W. Marsh, and J. Zagel, *Bull. Am. Phys. Soc.* **32**, 227 (1987).

<sup>8</sup>L. M. Young and R. I. Cutler, *IEEE Trans. Nucl. Sci.* **NS-32**, 1976 (1985).

<sup>9</sup>C. G. Yao, in Ref. 3, pp. 254–259.

<sup>10</sup>P. D. Goldan, *Phys. Fluids* **13**, 1055 (1970).

<sup>11</sup>D. A. Swanson, B. E. Cherrington, and J. T. Verdeyen, *Phys. Fluids* **16**, 1939 (1973).

<sup>12</sup>J. Shiloh, M. Lampel, and R. Sah, *Rev. Sci. Instrum.* **54**, 46 (1983).

<sup>13</sup>J. D. Jackson, *Classical Electrodynamics* (Wiley, New York, 1962).

<sup>14</sup>C. W. Mendel, Jr., *Rev. Sci. Instrum.* **46**, 847 (1975).

<sup>15</sup>FEI Company, 19500 N. W. Gibbs Dr., Ste. 100, Beaverton, OR 97006-6907.

<sup>16</sup>J. L. Wiza, "Microchannel Plate Detectors," Galileo Electro-Optics Corporation, Sturbridge, MA. Also, Data Sheets 9000 and 9200.